

<https://doi.org/10.1038/s43247-025-02275-4>

# Contemporaneous formation of self-secondaries and layered ejecta deposits on Mars



Fanglu Luo<sup>1</sup>, Zhiyong Xiao<sup>1,2</sup>✉, Rui Xu<sup>1</sup>, Yizhen Ma<sup>1</sup>, Yiren Chang<sup>3</sup>, Wei Cao<sup>1</sup>, Yichen Wang<sup>1</sup> & Jun Cui<sup>1,2</sup>

Self-secondaries are secondary craters formed in cogenetic ejecta deposits. Bearing important information on cratering mechanics and the applicability of remote age-determination technique using crater statistics, the spatial distribution of self-secondaries on Mars and their potential effect on martian crater chronology remain uncharacterized. Here, we show that self-secondaries are scarce on Mars, possessing minor effect on crater chronology. Recognized self-secondaries primarily occur on rim deposits and are largely absent on layered ejecta deposits, suggesting that the emplacement of self-secondaries and layered ejecta deposits occurred in a narrow time window. Comparison with model-predicted distributions of self-secondaries suggests that fragments forming self-secondaries did not uniformly have near-vertical ejection angles and may have slightly larger angles than those of normal excavation flows, explaining their common occurrence on airless planetary bodies. The double-layered ejecta of Steinheim ceased emplacement earlier than single- and multiple-layered ejecta, possibly due to the higher volatile content in pre-impact target materials.

The timeframe of martian geological and environmental evolution is mainly constrained by crater statistics<sup>1</sup>, as continual accumulation of impact craters enables remote age estimation for martian surfaces using the observed crater size-frequency distributions (SFDs) and an assumed impact flux. The impact flux on Mars is translated from that on the Moon<sup>2</sup>, because inner Solar System bodies may have experienced similar impactor populations<sup>3</sup> and the Moon is so far the only terrestrial body where samples with clear context information have been returned. Analysis of crater statistics on continuous ejecta deposits of impact craters is important in determining model ages for individual impact craters, and 5 of the 16 available calibration points for the lunar crater chronology came from crater statistics on continuous ejecta deposits of young lunar craters that are less than ~800 Ma old<sup>4–6</sup>.

Deriving representative crater production populations in continuous ejecta deposits of impact craters is not a straightforward task. While continuous ejecta deposits are formed simultaneously with their parent craters in geological terms, both their material properties (e.g., cohesive strength) and local resurfacing history by cogenetic ejecta flows are inherently heterogeneous<sup>7</sup>. On airless bodies, crater populations formed in continuous ejecta deposits of a given young crater usually exhibit large variations in spatial density<sup>8–10</sup>. The effect of target properties, that craters formed in

competent impact melt rocks are generally smaller than those formed in porous ballistic ejecta, could explain some of the observed discrepancies<sup>11</sup>. However, this effect cannot remedy all the observed differences of crater density<sup>12</sup>. For example, around a same crater, crater populations formed in different patches of melt pools<sup>9</sup> or debris flows<sup>13</sup> exhibit diverged densities.

On the other hand, there could be another major cause for the observed discrepant crater densities: self-secondaries, a subpopulation of craters formed by later-arriving fragments impacting earlier-emplaced fresh ejecta deposits around the parent crater<sup>8</sup>. Similar in shape and scattered spatial distributions with primary craters (primaries) of similar size, self-secondaries formed in continuous ejecta deposits are recognized on the basis of overlapping relationships with the other cogenetic ejecta facies, such as melt flows<sup>14</sup>. Self-secondaries have been observed on the Moon<sup>9,13,14</sup>, Mercury<sup>15</sup>, Mars<sup>16</sup>, 1 Ceres<sup>17</sup>, and icy satellites such as Rhea<sup>18</sup>. While fragments forming self-secondaries were interpreted to have ejection angles of larger than 80° (ref. 15), their ejection condition is not well constrained. Recent observations of the most proximal secondaries on terrestrial bodies show that, impact ejecta are capable of forming secondaries with ejection velocities of as small as ~25 m s<sup>-1</sup><sup>19</sup>, and ejection angles frequently change due to heterogeneous shock impedances<sup>20</sup>. Therefore, self-secondaries may be an inherent product of impact cratering on terrestrial bodies<sup>19</sup>, but their

<sup>1</sup>Planetary Environmental and Astrobiological Research Laboratory, School of Atmospheric Sciences, Sun Yat-sen University, Zhuhai, China. <sup>2</sup>Chinese Academy of Sciences Center for Excellence in Comparative Planetology, Hefei, China. <sup>3</sup>Mathematics and Science College, Shanghai Normal University, Shanghai, China.

✉e-mail: [xiaozhiyong@mail.sysu.edu.cn](mailto:xiaozhiyong@mail.sysu.edu.cn)

production rate was not well constrained, which is important for crater statistics in estimating ages of individual craters. This information is also crucial to refine the five Copernican-aged anchor points for the lunar crater chronology, as the possible effect of self-secondaries on resolvable production populations has not been determined yet<sup>10</sup>.

On Mars, the occurrence and spatial distribution of self-secondaries are not well resolved. So far, the only report of self-secondaries on Mars was based on asymmetric crater densities in the continuous ejecta deposits of Tooting<sup>16</sup>, as the southeastern crater rim exhibits both anomalously high crater density and possible evidence of infilling by melt flows (Fig. 1b). On the other hand, craters with layered ejecta deposits are widespread on Mars<sup>21</sup>. Although no consensus has been achieved yet on their possible emplacement mechanism(s), the subtly varying emplacement times of different ejecta layers and crosscutting relationships of different ejecta facies provide a unique opportunity to record the formation of self-secondaries (cf. <sup>22</sup>). In this work, we perform high-resolution geological observations and crater statistics for various ejecta facies around well-preserved impact craters on Mars to detect self-secondaries (Fig. 1a; see Methods).

## Occurrence of self-secondaries on Mars

Pristine simple and complex craters that have undergone little topographic degradation and with full coverage of high-resolution images are selected to investigate the occurrence of self-secondaries on Mars (Fig. 1a; Supplementary Table 1). Younger craters are not visible nearby to avoid superposing by younger chains and/or clusters of secondaries. The selected simple

craters were formed in late-Amazonian lava flows<sup>23,24</sup>, and they have obvious rays as seen in optical or thermal infrared images<sup>25</sup>. Six young complex craters with layered ejecta deposits are selected, and most of them have reported model ages of less than 10 Ma on the basis of crater statistics<sup>26,27</sup>. Layered ejecta deposits on Mars are classified as single-layered ejecta (SLE), double-layered ejecta (DLE), and multiple-layered ejecta (MLE) according to the number of visible ejecta layers<sup>28</sup>. Among the selected complex craters (Fig. 1a), Gratteri is a SLE crater; Steinheim and Bacolor are DLE craters, and Zunil, Tooting and Mojave are MLE craters. It is notable that DLE deposits on Mars are divided into two different groups: Type 1 and Type 2<sup>29</sup>. Type 2 DLE are similar to SLE and MLE, as the ejecta layers have high sinuosity, implying a similar formation mechanism<sup>29</sup>. Type 1 DLE deposits have more-or-less uniform radial extents for the inner ejecta layers<sup>29</sup>, and they may have different emplacement mechanism(s) than the other layered ejecta deposits<sup>22,27,30–32</sup>.

During impact cratering on planetary bodies, solid ejecta that formed secondaries were excavated from the transient cavities, via impact spallation and/or excavation flows<sup>33</sup>. For the investigated craters, their solid ejecta impacting the continuous ejecta deposits were theoretically capable of forming self-secondaries, considering that the minimum ballistic ranges of ejecta forming secondaries (~140 m) on Mars<sup>19</sup> are much smaller than the distances between rims of the transient cavities and final craters (140–9940 m; Supplementary Table 1). Meanwhile, solid ejecta with varying ejection velocities were excavated by the investigated craters, as evident by widespread typical chains of secondaries at larger radial distances<sup>19</sup>. Since target materials of planetary impacts naturally feature heterogeneous shock

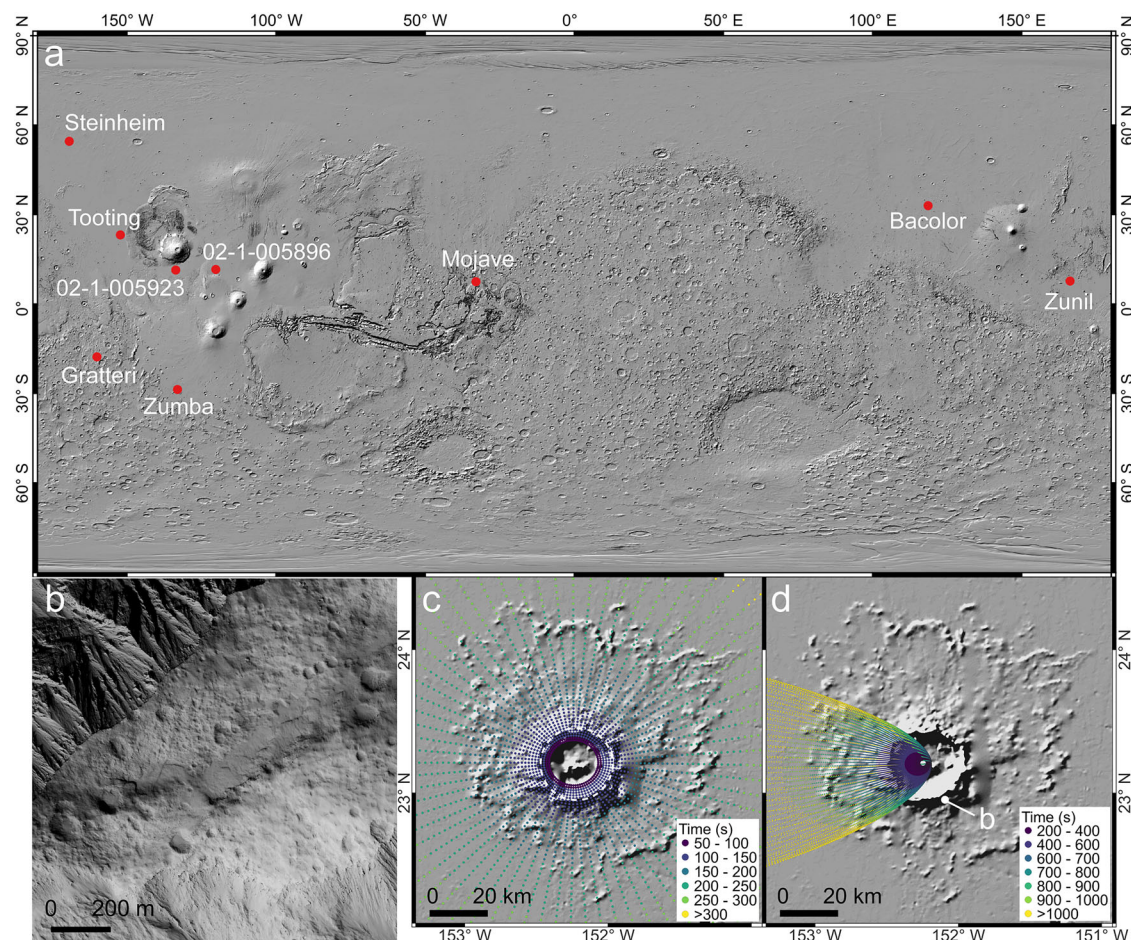


**Fig. 1 | Investigated martian craters and possible occurrence of self-secondaries around Tooting.** **a** Locations of martian craters investigated in this work (red dots). **b** Morphology of earlier-reported self-secondaries on the southeastern crater rim of Tooting<sup>16</sup>. The location is marked in (d). **c, d** Predicted landing positions of Tooting's

ejecta launched from the crater center with ejection angles  $\theta = 60^\circ$  and  $89^\circ$ , respectively. Modeled ejecta particles are color-coded according to their flight time (see Methods). The white dashed circle in (c) indicates the rim crest of Tooting. IDs and available addresses of base images used are in the Supplementary Table 2.



impedances caused by lithological and/or structural discontinuities, local propagation paths of shock and rarefaction waves experienced sporadic changes, so that variations of ejection velocities and/or angles are not rare for ejecta excavated from the same position<sup>20</sup>. Therefore, self-secondaries should have formed on the layered ejecta deposits<sup>19</sup>. If fragments forming self-secondaries had ejection angles ( $\theta$ ;  $0^\circ$  as surface tangent and  $90^\circ$  as surface normal) slightly larger than those launched by normal excavation flows ( $\theta = 35^\circ$ – $55^\circ$ ; ref. 34) and exhibited comparable ejection velocities ( $v$ ), they could be abundant on continuous ejecta deposits of young martian craters. For example, Fig. 1c shows the predicted impact sites of ballistic ejecta that have assumed ejection angles of  $\theta = 60^\circ$  around the MLE crater Tooting (rim crest diameter  $D = 29$  km; central coordinates of  $23.2^\circ\text{N}$ ,  $207.8^\circ\text{E}$ ). Instead, if self-secondaries were formed by fragments with near-vertical ejection angles (e.g.,  $\theta = 89^\circ$ ; ref. 10), they should preferentially occur in the western ejecta deposits due to the Coriolis effect (Fig. 1d; see Methods), regardless of locations of the parent craters (Supplementary Fig. 1).

Referring to theoretical estimations for thicknesses of proximal ejecta around martian craters (see Methods), younger craters formed in earlier-emplaced ejecta deposits are recognized, among which self-secondaries are identified if they were embayed by cogenetic impact melt deposits or transected by radial grooves in layered ejecta deposits (e.g., <sup>31</sup>; see Methods for details). Melt deposits in continuous ejecta deposits of martian craters are less obvious than those on the Moon, due to the lack of albedo contrast and typical flow fronts (Fig. 1b). Veneers and ponds of smooth deposits in continuous ejecta deposits were interpreted as either melt-rich ejecta<sup>16</sup> or aeolian deposits<sup>35</sup>. For smooth deposits that embayed younger craters in the continuous ejecta deposits, degassing pits<sup>36</sup> and cooling fractures<sup>37</sup> are used as diagnostic evidence for identifying cogenetic impact melt (see Methods).

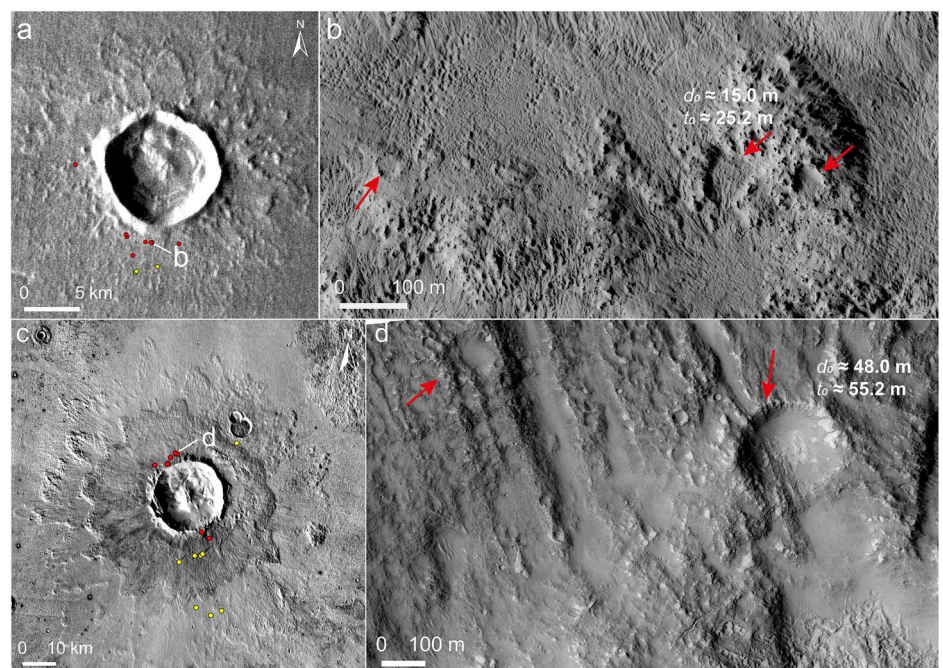
Our observations show that, unlike the dominance of self-secondaries in continuous ejecta deposits of young craters on the Moon and Mercury<sup>10</sup>, recognizable self-secondaries are scarce in the ejecta deposits of the young martian craters (Fig. 2 and Supplementary Figs. 2–3). With diameters of 25–466 m, the majority of the observed self-secondaries are located on rims of their parent craters, but they are not observed on the SLE or MLE deposits (Fig. 2a, b and Supplementary Fig. 3a–h). Instead, a handful of self-secondaries are recognized on the inner layers of the Type 1 DLE deposits (Fig. 2c, d and Supplementary Fig. 3i–k).

Self-secondaries on the Moon and Mercury exhibit nonuniform spatial distributions across the continuous ejecta deposits, evident by the varying

spatial densities of younger craters formed in smooth ejecta flows at different azimuths and radial distances<sup>9,13,15</sup>. Patches of smooth ejecta deposits are also widespread in SLE and MLE deposits of martian craters (Supplementary Fig. 4; ref. 26), but they are less abundant in ejecta deposits of the simple craters (Supplementary Fig. 5) and DLE craters<sup>32</sup>. We compare the spatial densities of crater populations formed in the smooth flow deposits at different azimuths and radial distances from rims of the parent craters, revealing no obvious differences in the crater SFDs (Fig. 3a–h). This observation confirms the above observation that self-secondaries are a negligible population in SLE or MLE deposits.

On the other hand, crater populations formed in the inner ejecta layer of the Type 1 DLE crater Steinheim exhibit non-uniform distribution, as the eastern part exhibits both clustered spatial distribution and larger densities than the entire inner ejecta layer (Fig. 3i–k and Supplementary Fig. 6). The observed crater populations consist of two or three components: primaries younger than Steinheim, self-secondaries of Steinheim (Supplementary Fig. 3i–k), and/or possible background secondaries formed by distal, younger craters. Considering the pristine morphology of Steinheim and absence of nearby younger craters, the contribution of background secondaries to the crater population on its layered ejecta deposits is expected to be minor. Assuming that potential distant background secondaries had uniform distribution across the entire inner ejecta unit<sup>13</sup>, we obtain an approximate production density of self-secondaries by subtracting the western crater population from the entire crater population in the inner ejecta layer (Fig. 3k). This approach yields a SFD for the extra-population of self-secondaries, which can be regarded as a minimum production density of self-secondaries in the inner ejecta layer. Referring to the Hartmann crater chronology<sup>2</sup>, the crater SFD for this extra-population of self-secondaries is equivalent to that of an  $\sim 22$  Ma isochron for primaries (Fig. 3k), which is unignorable compared to a model age of  $\sim 138$  Ma that is derived from the observable crater population on Steinheim (Supplementary Fig. 7). It is notable that only 4.2% of martian craters with  $D \geq 3$  km have DLE deposits<sup>23</sup>, among which six craters have Type 1 DLE deposits and formed in the Late Amazonian<sup>24</sup>, with Bacolor and Steinheim being the youngest cases<sup>27</sup>. Meanwhile, self-secondaries are a transient crater population formed together with the parent crater, and their SFD should be surpassed by the accumulation of subsequent craters, so that the proportion of self-secondaries in visible crater populations should decrease with time<sup>10</sup>. Therefore, our observations suggest that, away from rim crests of martian

**Fig. 2 | Occurrences of self-secondaries around young complex craters with layered ejecta deposits on Mars. a, c** Context of Zunil and Bacolor craters, respectively. Red and yellow dots indicate the locations of confirmed self-secondaries and possible self-secondaries, respectively. **b, d** Morphology of confirmed self-secondaries (indicated by red arrows) that are embayed or transected by other ejecta facies is shown for each crater. Their locations are marked in corresponding (a, c). Theoretical estimations for the initial rim-to-floor depths of confirmed self-secondaries ( $d_0$ ) and thicknesses of ejecta formed by the source crater ( $t_0$ ) are compared (see Methods), showing that the self-secondaries postdated the emplacement of the underlying ejecta. In (b, d),  $d_0$  and  $t_0$  for the largest self-secondary crater within the displayed frames are presented as examples, given the comparable thicknesses of ejecta for these self-secondaries. IDs and available addresses of base images used are in the Supplementary Table 2.



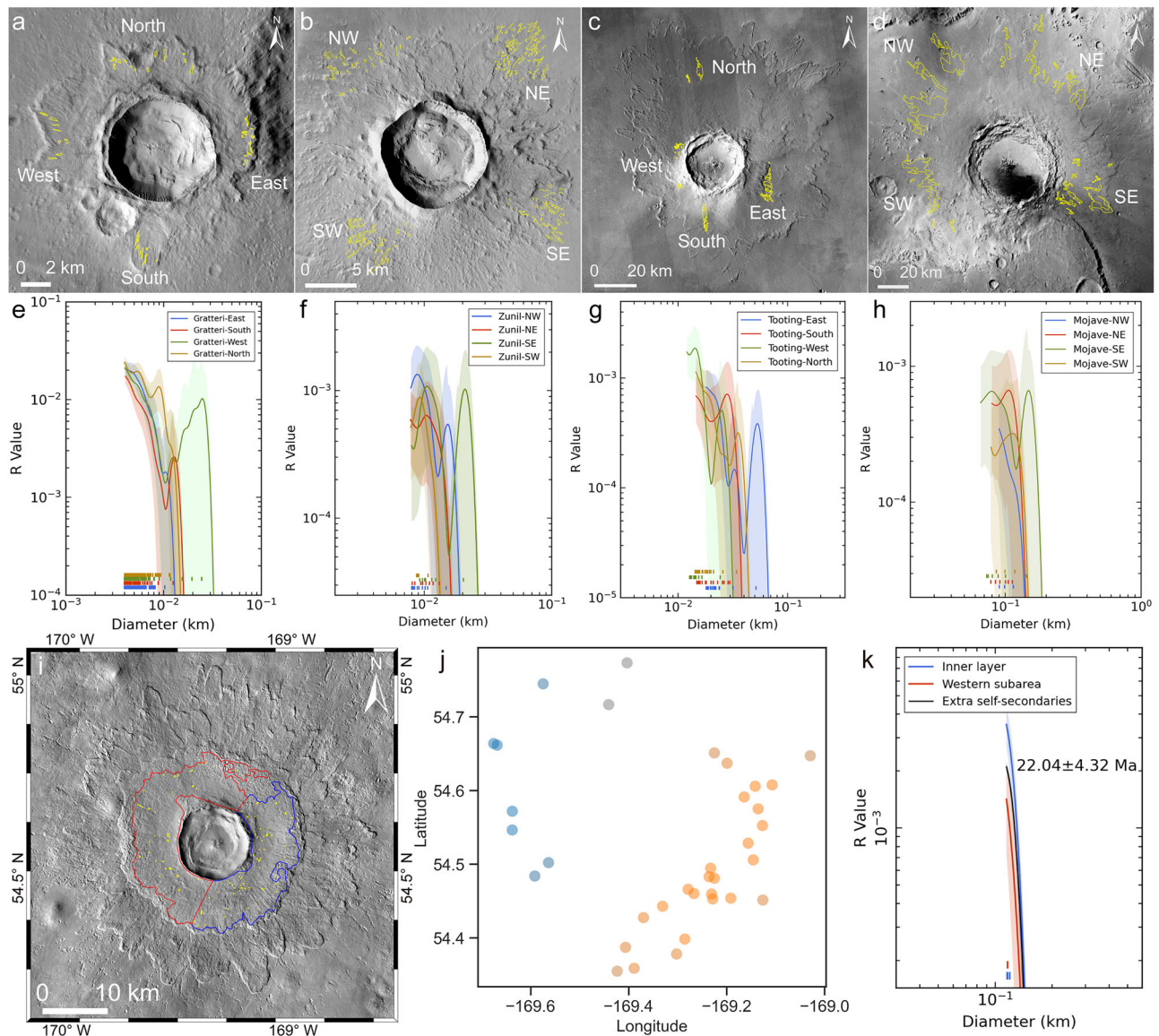


**Fig. 3 | Size-frequency distributions of craters formed on layered ejecta deposits on Mars.** **a–h** show counting areas (yellow polygons in **a–d**) and size-frequency distributions (**e–h**) of crater populations formed in smooth deposits of single- or multiple-layered ejecta (SLE or MLE). Gratteri has SLE deposits (**a, e**), and Zunil (**b, f**), Tooting (**c, g**), and Mojave (**d, h**) have MLE deposits. **i** Counting areas (red and blue polygons) and craters (yellow circles) collected on the inner ejecta layer of Steinheim, which is a Type 1 double-layered ejecta (DLE) crater. The red polygon is for the western half of the inner ejecta layer, and it overlaps the blue polygon that is for the entire inner ejecta layer. **j** Cluster analysis for the crater population formed in the inner layer revealing a clustered distribution for craters with  $D = 95\text{--}120\text{ m}$  in the eastern half. Dots represent the locations of craters collected in the inner ejecta layer.

Colors saturation is based on the strength of membership, with dark being strong and light being weak (see Methods). Craters in the same cluster have the same color, and unclustered craters are gray. Analyses of spatial distribution of the entire crater population are shown in Supplementary Fig. 6. **k** Size-frequency distributions of the  $D = 95\text{--}120\text{ m}$  craters in the entire (blue) and western half (red) of the inner ejecta layer. The approximate population of the extra self-secondaries (black curve) is derived by subtracting the western crater population from the entire crater population in the inner ejecta layer. The equivalent model age for the population of extra self-secondaries is derived using the Hartmann crater chronology<sup>2</sup>. The 95% confidence interval is represented by color shades in (**e–h**) and (**k**) (see Methods). IDs and available addresses of base images used are in the Supplementary Table 2.

craters, crater statistics on the continuous ejecta deposits are not obviously affected by self-secondaries, except for the few young craters with Type 1 DLE deposits, lending support to the applicability of crater statistics to estimate their model ages.

### Near-contemporaneous emplacement of self-secondaries and layered ejecta deposits

Unlike the predicted landing positions for near-vertically launched ejecta (i.e.,  $\theta = 89^\circ$ ; Fig. 1d and Supplementary Fig. 1), the observed self-secondaries do not avoid occurring on the eastern rims or ejecta deposits of the investigated craters (Fig. 2 and Supplementary Figs. 2–3). Therefore, with longer trajectory times than ejecta forming the underlying

ballistic ejecta deposits<sup>10</sup>, ejecta forming self-secondaries did not uniformly have near-vertical ejection angles<sup>19</sup>. On the other hand, in contrast to the predicted landing positions of ejecta with slightly larger ejection angles than normal excavation flows (Fig. 1c and Supplementary Fig. 1), the observed self-secondaries avoid occurring on layered ejecta deposits but preferentially occur on crater rims (Fig. 2 and Supplementary Fig. 3). Considering that impacts of ballistic ejecta and emplacement of layered ejecta deposits occurred near contemporaneously during the formation of the parent crater<sup>7,21,33,38</sup>, most self-secondaries should have formed during the emplacement of layered ejecta deposits and were destroyed by the advancing ejecta layers. This interpretation further suggests that the duration of emplacement of SLE and MLE deposits should be



comparable to or slightly longer than flight times of fragments forming self-secondaries.

While the formation of self-secondaries occurred simultaneously with the emplacement of SLE and MLE, the prominent existence of self-secondaries on Type 1 DLE deposits, although not abundant (Fig. 2c), indicates that DLE was emplaced slightly earlier than SLE and MLE. This interpretation suggests that self-secondaries may not be entirely destroyed due to the earlier emplacement of DLE, and those formed later on the inner ejecta layer were subsequently transected by radial grooves (Fig. 2d). The earlier emplacement of Type 1 DLE is supported by the observation that, SLE and MLE deposits inundated earlier-formed cogenetic chains of secondaries (Supplementary Fig. 8; ref. 39), whereas pristine chains of secondaries were preserved on the outer ejecta layer of the Type 1 DLE (Supplementary Fig. 9). The pre-impact target of Type 1 DLE craters contained larger amounts of volatiles such as water ice<sup>22</sup>, because these craters preferentially occur in the mid-high latitudes of Mars<sup>39</sup>, where non-polar surface snow and ice were deposited in the late-Amazonian<sup>40</sup>. Sublimation pits, ring-mold craters, and expanded secondaries formed due to the loss of subsurface water ice are also commonly seen in Type 1 DLE deposits<sup>22,41–44</sup>. Therefore, it is possible that more volatiles were excavated by impacts that formed the Type 1 DLE craters (cf. <sup>22</sup>), and ice and/or water lubrication of the ejecta led to their larger emplacement speeds and thus earlier emplacement than SLE and MLE deposits.

### Emplacement speeds of layered ejecta deposits

Emplacement speeds of layered ejecta deposits on Mars are not constrained yet, which are important to the understanding of their formation mechanisms<sup>45,46</sup>. Earlier morphological study suggested that SLE, MLE, Type 2 DLE, and outer ejecta layers of Type 1 DLE may have similar emplacement mechanism<sup>22,47–50</sup>. The contrasting occurrence of self-secondaries on the layered ejecta deposits further shows that the outer ejecta layer of Steinheim ceased emplacement earlier than the SLE and MLE. The outer ejecta layer of Steinheim appears as a continuous sheet of flow deposits (Supplementary Fig. 9), which is covered by the later-emplaced inner ejecta layer<sup>22,27</sup>. Well-preserved chains of secondaries (~7 km long) formed on the outer ejecta layer, and fragments forming chains of secondaries were mostly launched from about half radius of the transient cavity<sup>19</sup>. Referring to the maximum possible flow distances of the outer ejecta layer that extended from the transient cavity rim<sup>45</sup>, the ballistic ranges of ejecta that formed the chains of secondaries are used to estimate the minimum emplacement speed of the ejecta flow, which is 112–160 m s<sup>-1</sup> (see Supplementary Text 1 for detailed calculation). Considering frictional deceleration during emplacement, the emplacement speed of the outer ejecta layer may be even larger, substantially exceeding typical movement speeds of long-runout landslides on Mars (~30 m s<sup>-1</sup>; refs. 51,52).

Referring to the theoretical flight times of ejecta that were capable of forming self-secondaries at comparable trajectory ranges, emplacement speeds of SLE and MLE are loosely constrained. Assuming that ejecta forming self-secondaries had ejection angles of  $\theta = 60^\circ$ – $80^\circ$ , larger than those of excavation flows that formed the continuous ejecta deposits and chains of secondaries<sup>10,34</sup>, the modeled flight times vary widely. Specifically, for  $\theta = 60^\circ$ , ejecta with trajectory ranges reaching the layered ejecta deposits had maximum flight times of 93–291 s (Fig. 1c and Supplementary Fig. 1). These times increase to ~110–375 s for  $\theta = 70^\circ$  (Supplementary Fig. 10) and ~159–567 s for  $\theta = 80^\circ$  (Supplementary Fig. 11). Referring to radial extensions of the investigated layered ejecta deposits from rim crests of their parent craters (Supplementary Table 1), the average emplacement speeds of SLE and MLE can be estimated to range from ~19 m s<sup>-1</sup> to as high as ~200 m s<sup>-1</sup>, depending on the assumed ejection angles. Therefore, while SLE and MLE ceased emplacement later than the Type-1 DLE of Steinheim, their emplacement speeds are not well constrained.

### Synthesis of emplacement sequences of proximal ejecta on Mars

The distribution of self-secondaries establishes a key bridge that synthesizes the deposition sequences for various forms of proximal ejecta around martian craters (Fig. 4). Emplacement of layered ejecta initiated during the modification of the transient cavity and the landing of ballistic ejecta, which may be accompanied by other mass movements, such as melt flows pushed out from transient cavity<sup>7</sup>, local excavation and/or ground-hugging flows triggered by landing of ejecta<sup>19,21,38,50,53</sup>. Affected by different contents of volatiles in pre-impact targets, movement speeds of layered ejecta are variable, and those of the Type 1 DLE deposits (e.g., those of Steinheim) are substantially larger than movement speeds of long-runout landslides on Mars. Therefore, at larger distances, layered ejecta deposits may either arrive earlier or later than fragments that formed cogenetic chains of secondaries (Fig. 4c). During the emplacement of layered ejecta deposits, fragments with larger ejection angles than normal excavation flows re-impacted the surface, but most self-secondaries formed on the layered ejecta deposits were destroyed by the advancing ejecta deposits (Fig. 4c, d). Rim-crests of the parent craters and inner ejecta layers of Type 1 DLE were settled earlier during the emplacement of the ejecta layers, where self-secondaries are preferentially preserved (Fig. 4d).

Radial grooves were developed after the emplacement of inner ejecta layer of Type 1 DLE, transecting self-secondaries (Fig. 2, d). With much smaller depths than thicknesses of the inner ejecta layer (Fig. 2d), the radial grooves are not equivalent to longitudinal grooves developed in martian landslides, which were referred to interpret that the inner ejecta layer was formed via landslides<sup>22,27</sup>. Alternatively, the observed shallow transection of self-secondaries by the radial grooves (Fig. 2d) supports that the radial grooves were scoured by fine debris that were engulfed as either base surges fed by fuel-coolant explosions<sup>30,54</sup> and/or the collapse of impact-generated debris-rich plumes<sup>31</sup>.

### Methods

#### Usage of remote sensing data

We mainly use calibrated data acquired by the High-Resolution Imaging Science Experiment (HiRISE; 0.25 m/pixel; ref. 55), the Context Camera (CTX; ~5 m/pixel; ref. 56), and the Thermal Emission Imaging System (THEMIS; ~100 m/pixel; ref. 57) for detailed geological investigations and crater statistics. Various other regional and global datasets are also used for assistance, such as high-resolution digital elevation models for specific impact craters, the Murray Lab CTX global mosaic<sup>58</sup>, and the Mars Orbiter Laser Altimeter (MOLA; ref. 59) global topography model. Supplementary Table 2 shows the basic information for the remote sensing data used in this work.

#### Revealing the spatial distribution of self-secondaries

Due to the rough topography of continuous ejecta deposits of martian impact craters, the identification of self-secondaries on Mars is more challenging than that on the Moon and Mercury. To ensure the reliability of observational results, we establish rigorous criteria for identifying self-secondaries, so that the cataloged cases are conservative. To exclude pre-existing craters, younger craters formed in earlier-emplaced ejecta deposits are identified if their assumed initial depths (i.e., 0.2 of the measured diameters; ref. 33) are less than the ejecta thickness (Fig. 2 and Supplementary Figs. 2–3). The thickness of the ejecta at certain location is estimated using the empirical scaling laws for martian craters (Supplementary Text 2; ref. 60). For younger craters formed in ejecta deposits, transection relationships with other cogenetic ejecta facies (e.g., impact melt deposits and radial grooves) are used to identify self-secondaries. Impact melt deposits are recognized based on the presence of degassing pits (e.g., Fig. 2b), typical cooling fractures (e.g., Supplementary Fig. 3d), and flow fronts (e.g., Supplementary Fig. 3e). Degassing pits are commonly developed in melt-rich ejecta on Mars<sup>36</sup>. Individual degassing pits may resemble similar-sized secondaries, but their spatial distributions that are more clustered than

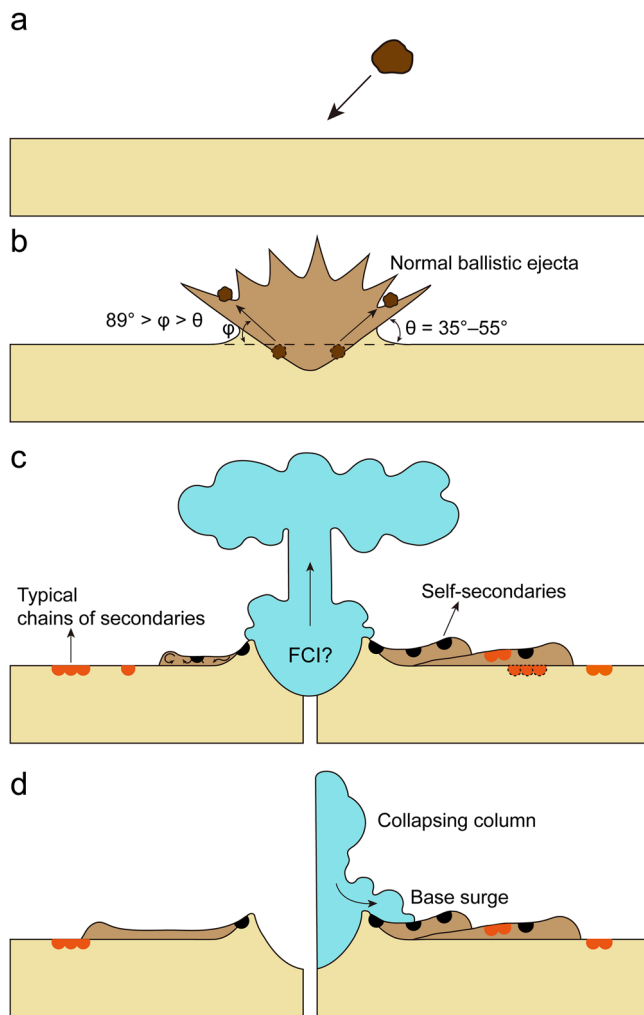


**Fig. 4 | A schematic diagram for the formation sequences of chains of secondaries (orange dots), self-secondaries (black dots), and layered ejecta deposits (brown polygons) on Mars.** Profile dimension is not to scale. The left panels are for single- and multiple-layered ejecta (SLE and MLE) deposits, and also possibly for the Type 2 double-layered ejecta (DLE) deposits<sup>29</sup>. The right panels are for the Type 1 DLE deposits. **a, b** The early contact and excavation processes are similar for craters with different types of layered ejecta deposits. Fragments forming self-secondaries have larger ejection angles ( $\phi$ ) than normal ballistic ejecta that were ejected by excavation flows ( $\theta = 35^\circ\text{--}55^\circ$ ). **c** Contemporaneous formation of most self-secondaries and emplacement of layered ejecta deposits. Both the inner and outer ejecta layers of DLE were emplaced earlier than SLE and MLE, and the latter may contain internal turbulence that has destroyed contemporaneously formed self-secondaries. Typical chains of secondaries are usually covered by layered ejecta deposits, but the outer ejecta layer of some DLE may arrive before chains of secondaries were formed (brown polygons). Possible impact plume (blue shade) and fuel-coolant interaction (FCI) caused by the interaction between hot impactite and volatiles<sup>54</sup> may exist during the emplacement of layered ejecta deposits. **d** Most self-secondaries that once formed in SLE and MLE deposits of martian craters were destroyed by the emplacement of the layered ejecta, and the observed ones are mainly located on crater rims and other ballistic ejecta that were not destroyed by layered ejecta deposits. DLE deposits ceased movement earlier than SLE and MLE, so that the last-formed self-secondaries were preserved in DLE, especially in the inner layer. The collapse of the impact plume and/or debris flows triggered by FCI occurred after layered ejecta deposits were emplaced, forming radial grooves that transect self-secondaries in the inner ejecta layer.

typical chains and clusters of secondaries (Supplementary Fig. 12). In addition, craters formed in layered ejecta deposits are tagged as self-secondaries if they are transected by radial grooves that develop in inner ejecta layers of Type 1 DLE deposits<sup>30</sup>. It is notable that aeolian deposits are pervasive on Mars (e.g., reticulate ridges; ref. 61) (Supplementary Fig. 13),

and their smooth morphology and textures are similar with potential melt-rich veneers (Supplementary Fig. 14; ref. 35). Therefore, for small craters buried by smooth deposits that resemble melt flows, the possibility that the flooded deposits being aeolian deposits cannot be ruled out. Such small craters are tagged as possible self-secondaries (e.g., yellow dots in Supplementary Fig. 2). In addition, craters that exhibit embayment and/or transection relationships with other ejecta facies but with initial rim-to-floor depths larger than theoretical estimations of local ejecta thickness (see Supplementary Text 2) are also categorized as unconfirmed self-secondaries (Fig. 2 and Supplementary Figs. 2–3).

To investigate the spatial distribution of self-secondaries around the selected craters, we compare crater SFDs at multiple locations on their continuous ejecta deposits. For young craters on airless bodies, only a portion of self-secondaries can be recognized on the basis of unambiguous overlapping relationships with other ejecta facies<sup>13</sup>, and many self-secondaries occur as scattered circular craters that are not differentiated from same-sized primaries or distal background secondaries<sup>15</sup>. High-resolution crater statistics are a valuable method to detect the possible existence of such self-secondaries<sup>9,13</sup>, but the effect of complicated topography on crater counting, such as aeolian dunes, massifs, and degassing pits, cannot be ignored<sup>62,63</sup>. Therefore, on the basis of high-resolution geological observation for the continuous ejecta deposits, we select long and continuous smooth ejecta deposits that are located at different azimuths and radial distances to compare the SFDs of superposed craters. Such smooth surfaces occur as superficial veneers in continuous ejecta deposits, and they might be rich in impact melt (Supplementary Fig. 4). Selection criteria of counting areas and technical details of crater statistics are shown in the Supplementary Text 3. The minimum confidence diameter for completeness is set to be at least 10 pixels of the base image used for crater statistics<sup>64</sup>, and the arithmetic square root of the minimum confidence counting area is set to be 200 times greater than the minimum confidence diameter to ensure reliable statistics<sup>65</sup>. Considering the average width of radial grooves in the inner ejecta layer of Steinheim, i.e., ~95 m<sup>30</sup>, the minimum confident diameter for completed crater statistics on this layer is set to be 95 m (Fig. 3i–k). The Supplementary Table 1 summarizes the basic information for crater statistics done in this work. Following the statistical method advocated by Robbins et al.<sup>66</sup>, we use a Gaussian kernel density estimator to derive the crater SFDs, a bootstrap sampling to estimate the confidence interval for the SFD, and a maximum likelihood estimator to derive model ages based on the Hartmann crater chronology (Supplementary Text 3; ref. 2). The Crater Analysis Techniques Working Group<sup>67</sup> advised different algorithms to display crater SFDs, such as cumulative, relative, differential, and incremental plots. Among the different methods, relative plots (i.e.,  $R$  plots) better show subtle changes of SFD slopes<sup>67</sup>, and this method is used in this work to compare the shapes of crater SFDs at different azimuths (Fig. 3e–h). Cumulative plots are conventionally used to derive model ages based on a crater chronology system (e.g.,<sup>68</sup>), and this method is used in this work to predict model ages for the observed crater populations (Supplementary Fig. 7).

We perform spatial analysis for the collected crater populations to detect possibly clustered spatial distribution of self-secondaries. While self-secondaries exhibit morphologies comparable to primaries of the same size, those on the Moon frequently show clustered spatial distributions at regional scales<sup>13</sup>. A hierarchical clustering algorithm, density-based spatial clustering of applications with noise (HDBSCAN), is employed for this analysis<sup>69</sup>. HDBSCAN enables identification of clusters with varying spatial densities, which is well suited for planetary landforms such as impact craters<sup>70</sup> and volcanoes<sup>71</sup>.

### Ballistic trajectory modeling for fragments that formed self-secondaries

On the basis of the observed occurrences of self-secondaries and their emplacement sequences with other cogenetic ejecta facies (e.g., layered ejecta deposits and chains of secondaries), we compare the observations with model-predicted landing positions and flight times of ballistic ejecta to

investigate the ejection conditions of fragments that formed self-secondaries. The smallest self-secondaries observed in this study are ~25 m in diameter. According to the cratering scaling laws of Holsapple<sup>72</sup>, fragments that formed the observed self-secondaries have minimum sizes of ~180 cm when assuming the maximum cratering efficiency, i.e.,  $\theta = 89^\circ$ ,  $v = 5.03 \text{ km s}^{-1}$  that equals the escape velocity of Mars, and both impactor and target being competent basalts with a density of  $3.0 \text{ g cm}^{-3}$ . Ballistic trajectories of fragments larger than ~40 cm are not substantially affected by atmospheric drag in the current martian atmosphere<sup>73,74</sup>. Therefore, we employ the algorithm of Xu et al.<sup>20</sup> to model the ballistic trajectory for fragments that are capable of forming self-secondaries. This model considers the effect of planetary rotation on ballistic trajectories, and ejecta launched from the crater center with varying azimuths,  $\theta$ , and  $v$  are modeled. Here, the flight time of ejecta is likely overestimated, as the empirical ejecta launch positions are typically located at about half the transient crater radius of the parent crater<sup>19</sup>. Each simulation has a fixed  $\theta$  that varies from  $35^\circ$  to  $89^\circ$ , and more than 10,000 ejecta particles are seeded with uniform distributions of  $v = 0.2\text{--}5.03 \text{ km s}^{-1}$  (the lower limit is larger than the minimum landing velocity of ejecta to form secondaries<sup>19</sup>) and ejection azimuths of  $0^\circ\text{--}360^\circ$  ( $0^\circ$  is local north and  $90^\circ$  is local east). The landing positions and flight times of the simulated particles are recorded.

## Data availability

Data used in this study are in the public domain and their IDs and available addresses are summarized in the Supplementary Table 2. Raw data generated in this study, including all the counting areas and crater statistics, are open to the public at <https://doi.org/10.5281/zenodo.10083548><sup>75</sup>.

## Code availability

The code used for plotting crater SFDs and confidence intervals is provided by Robbins et al.<sup>66</sup>, while the code for modeling the ballistic trajectory of impact ejecta on rotated planetary bodies is provided by Xu et al.<sup>20</sup>.

Received: 11 January 2024; Accepted: 4 April 2025;

Published online: 12 April 2025

## References

- Werner, S. C. & Ivanov, B. A. Exogenic dynamics, cratering, and surface ages. *Treatise Geophys.* 327–365 (Elsevier, <https://doi.org/10.1016/B978-0-444-53802-4.00170-6>). (2015).
- Hartmann, W. K. Martian cratering 8: isochron refinement and the chronology of Mars. *Icarus* **174**, 294–320 (2005).
- Strom, R. G., Malhotra, R., Ito, T., Yoshida, F. & Kring, D. A. The origin of planetary impactors in the inner solar system. *Science* **309**, 1847–1850 (2005).
- Cui, Z. et al. A sample of the Moon's far side retrieved by Chang'e-6 contains 2.83-billion-year-old basalt. *Science* **386**, 1395–1399 (2024).
- Neukum, G., Ivanov, B. A. & Hartmann, W. K. Cratering records in the inner solar system in relation to the lunar reference system. in *Chronology and Evolution of Mars* (eds. Kallenbach, R., Geiss, J. & Hartmann, W. K.) 55–86 (Springer, 2001).
- Xie, M. & Xiao, Z. A new chronology from debiased crater densities: Implications for the origin and evolution of lunar impactors. *Earth Planet. Sci. Lett.* **602**, 117963 (2023).
- Osinski, G. R., Tornabene, L. L. & Grieve, R. A. F. Impact ejecta emplacement on terrestrial planets. *Earth Planet. Sci. Lett.* **310**, 167–181 (2011).
- Shoemaker, E. M. et al. Observations of the lunar regolith and the Earth from the television camera on Surveyor 7. *J. Geophys. Res.* **74**, 6081–6119 (1969).
- Zanetti, M. et al. Evidence for self-secondary cratering of Copernican-age continuous ejecta deposits on the Moon. *Icarus* **298**, 64–77 (2017).
- Xiao, Z. On the importance of self-secondaries. *Geosci. Lett.* **5**, 17 (2018).
- van der Bogert, C. H. et al. Origin of discrepancies between crater size-frequency distributions of coeval lunar geologic units via target property contrasts. *Icarus* **298**, 49–63 (2017).
- Xiao, Z. & Werner, S. C. Size-frequency distribution of crater populations in equilibrium on the Moon. *JGR Planets* **120**, 2277–2292 (2015).
- Chang, Y., Xiao, Z., Liu, Y. & Cui, J. Self-secondaries formed by cold spot craters on the Moon. *Remote Sensing* **13**, 1087 (2021).
- Plescia, J., Robinson, M. & Paige, D. Giordano Bruno: the young and the restless. In *41st Annual Lunar and Planetary Science Conference* 2038 (Lunar and Planetary Institute, 2010).
- Xiao, Z., Prieur, N. C. & Werner, S. C. The self-secondary crater population of the Hokusai crater on Mercury. *Geophys. Res. Lett.* **43**, 7424–7432 (2016).
- Boyce, J. & Mouginis-Mark, P. Anomalous areas of high crater density on the rim of the Martian crater Tooting. *Issue Crater Stud. Dating Planet. Surf.* **1841**, 9005 (2015).
- Neesemann, A. et al. The various ages of Occator crater, Ceres: Results of a comprehensive synthesis approach. *Icarus* **320**, 60–82 (2019).
- Schenk, P., Kirchoff, M., Hoogenboom, T. & Rivera-Valentín, E. The anatomy of fresh complex craters on the mid-sized icy moons of Saturn and self-secondary cratering at the rayed crater Inktomi (Rhea). *Meteorit. Planet. Sci.* **55**, 2440–2460 (2020).
- Xu, R., Xiao, Z., Wang, Y., Luo, F. & Ma, Y. Minimum velocity for impact ejecta to form secondaries on terrestrial bodies. *Commun. Earth Environ.* **5**, 641 (2024).
- Xu, R., Xiao, Z., Luo, F., Wang, Y. & Cui, J. Untrackable distal ejecta on planetary surfaces. *Nat. Commun.* **14**, 1173 (2023).
- Carr, M. H. et al. Martian impact craters and emplacement of ejecta by surface flow. *J. Geophys. Res.* **82**, 4055–4065 (1977).
- Weiss, D. K. & Head, J. W. Testing landslide and atmospheric-effects models for the formation of double-layered ejecta craters on Mars. *Meteorit. Planet. Sci.* **53**, 741–777 (2018).
- Robbins, S. J. & Hynek, B. M. A new global database of Mars impact craters  $\geq 1 \text{ km}$ : 1. Database creation, properties, and parameters. *J. Geophys. Res.* **117**, 2011JE003966 (2012).
- Tanaka, K. L., Robbins, S. J., Fortezzo, C. M., Skinner, J. A. & Hare, T. M. The digital global geologic map of Mars: chronostratigraphic ages, topographic and crater morphologic characteristics, and updated resurfacing history. *Planet. Space Sci.* **95**, 11–24 (2014).
- Harris, J. K., McKeown, L. E., Parenti, C., Tornabene, L. L. & Grindrod, P. M. An updated catalog of rayed craters on Mars. *Earth Space Sci.* **10**, e2021EA001814 (2023).
- LUO, F. et al. The source crater of depleted shergottites. *Acta Geol. Sini. English Edition* **98**, 1672–1681 (2024).
- Wulf, G. & Kenkmann, T. High-resolution studies of double-layered ejecta craters: Morphology, inherent structure, and a phenomenological formation model. *Meteorit. Planet. Sci.* **50**, 173–203 (2015).
- Barlow, N. G. et al. Standardizing the nomenclature of Martian impact crater ejecta morphologies. *J. Geophys. Res.* **105**, 26733–26738 (2000).
- Barlow, N. G. Characteristics of impact craters in the northern hemisphere of Mars. In *Geological Society of America Special Papers* (Geological Society of America, 2015).
- Boyce, J. M. & Mouginis-Mark, P. J. Morphologic differences in radial grooves on martian layered (fluidized) ejecta: implications for emplacement processes and conditions. *Icarus* **366**, 114513 (2021).
- Boyce, J. M. & Mouginis-Mark, P. J. Martian craters viewed by the Thermal Emission Imaging System instrument: Double-layered ejecta craters. *J. Geophys. Res.* **111**, 2005JE002638 (2006).
- Cao, W., Xiao, Z., Luo, F., Ma, Y. & Xu, R. Comparison of topographic roughness of layered deposits on Mars. *Remote Sens.* **15**, 2272 (2023).



33. Melosh, H. J. *Impact cratering: a geologic process* (Oxford University Press, 1989).
34. Anderson, J. L. B., Schultz, P. H. & Heineck, J. T. Asymmetry of ejecta flow during oblique impacts using three-dimensional particle image velocimetry. *J. Geophys. Res.* **108**, 2003JE002075 (2003).
35. Golombek, M. P. et al. Erosion rates at the Mars Exploration Rover landing sites and long-term climate change on Mars. *J. Geophys. Res. Planets* **111**, E12 (2006).
36. Tornabene, L. L. et al. Widespread crater-related pitted materials on Mars: further evidence for the role of target volatiles during the impact process. *Icarus* **220**, 348–368 (2012).
37. Xiao, Z., Zeng, Z., Li, Z., Blair, D. M. & Xiao, L. Cooling fractures in impact melt deposits on the Moon and Mercury: implications for cooling solely by thermal radiation. *J. Geophys. Res. Planets* **119**, 1496–1515 (2014).
38. Oberbeck, V. R. The role of ballistic erosion and sedimentation in lunar stratigraphy. *Rev. Geophys.* **13**, 337–362 (1975).
39. Kirchoff, M. R. & Grimm, R. E. Timing and distribution of single-layered ejecta craters imply sporadic preservation of tropical subsurface ice on Mars. *J. Geophys. Res. Planets* **123**, 131–144 (2018).
40. Head, J. W., Mustard, J. F., Kreslavsky, M. A., Milliken, R. E. & Marchant, D. R. Recent ice ages on Mars. *Nature* **426**, 797–802 (2003).
41. Kadish, S. J., Head, J. W., Barlow, N. G. & Marchant, D. R. Martian pedestal craters: marginal sublimation pits implicate a climate-related formation mechanism. *Geophys. Res. Lett.* **35**, 16 (2008).
42. Kress, A. M. & Head, J. W. Ring-mold craters in lineated valley fill and lobate debris aprons on Mars: evidence for subsurface glacial ice. *Geophys. Res. Lett.* **35**, 23 (2008).
43. Viola, D., McEwen, A. S., Dundas, C. M. & Byrne, S. Subsurface volatile content of martian double-layer ejecta (DLE) craters. *Icarus* **284**, 325–343 (2017).
44. Viola, D., McEwen, A. S., Dundas, C. M. & Byrne, S. Expanded secondary craters in the Arcadia Planitia region, Mars: evidence for tens of Myr-old shallow subsurface ice. *Icarus* **248**, 190–204 (2015).
45. Baloga, S. M., Fagents, S. A. & Mougini-Mark, P. J. Emplacement of Martian rampart crater deposits. *J. Geophys. Res.* **110**, 2004JE002338 (2005).
46. Barnouin-Jha, O. S., Baloga, S. & Glaze, L. Comparing landslides to fluidized crater ejecta on Mars. *J. Geophys. Res.* **110**, 2003JE002214 (2005).
47. Mougini-Mark, P. Ejecta emplacement and modes of formation of martian fluidized ejecta craters. *Icarus* **45**, 60–76 (1981).
48. Schultz, P. H. Atmospheric effects on ejecta emplacement. *J. Geophys. Res.* **97**, 11623–11662 (1992).
49. Barlow, N. G. Impact craters in the northern hemisphere of Mars: Layered ejecta and central pit characteristics. *Meteorit Planet. Sci.* **41**, 1425–1436 (2006).
50. Komatsu, G., Ori, G. G., Di Lorenzo, S., Rossi, A. P. & Neukum, G. Combinations of processes responsible for Martian impact crater “layered ejecta structures” emplacement. *J. Geophys. Res.* **112**, 2006JE002787 (2007).
51. Lucchitta, B. K. A large landslide on Mars. *Geol. Soc. Am. Bull.* **89**, 1601 (1978).
52. Quantin, C., Allemand, P. & Delacourt, C. Morphology and geometry of Valles Marineris landslides. *Planet. Space Sci.* **52**, 1011–1022 (2004).
53. Wada, K. & Barnouin-Jha, O. S. The formation of fluidized ejecta on Mars by granular flows. *Meteoritics Planet. Sci.* **41**, 1551–1569 (2006).
54. Artemieva, N., Wünnemann, K., Krien, F., Reimold, W. & Stöffler, D. Ries crater and suevite revisited—Observations and modeling Part II: Modeling. *Meteoritics Planet. Sci.* **48**, 590–627 (2013).
55. McEwen, A. S. et al. Mars reconnaissance orbiter’s high resolution imaging science experiment (HiRISE). *J. Geophys. Res. Planets* **112**, E5 (2007).
56. Malin, M. C. et al. Context camera investigation on board the Mars Reconnaissance Orbiter. *J. Geophys. Res. Planets* **112**, E5 (2007).
57. Christensen, P. R. et al. The thermal emission imaging system (THEMIS) for the Mars 2001 Odyssey Mission. *Space Sci. Rev.* **110**, 85–130 (2004).
58. Dickson, J., Kerber, L., Fassett, C. & Ehlmann, B. A global, blended CTX mosaic of Mars with vectorized seam mapping: a new mosaicking pipeline using principles of non-destructive image editing. in *Lunar and planetary science conference* vol. 49 1–2 (Lunar and Planetary Institute The Woodlands, 2018).
59. Zuber, M. T. et al. The Mars Observer laser altimeter investigation. *J. Geophys. Res. Planets* **97**, 7781–7797 (1992).
60. Garvin, J. B. & Frawley, J. J. Geometric properties of Martian impact craters: preliminary results from the Mars Orbiter Laser Altimeter. *Geophys. Res. Lett.* **25**, 4405–4408 (1998).
61. Bridges, N. T. et al. Aeolian bedforms, yardangs, and indurated surfaces in the Tharsis Montes as seen by the HiRISE Camera: Evidence for dust aggregates. *Icarus* **205**, 165–182 (2010).
62. Luo, F. et al. The Production Population of Impact Craters in the Chang’E-6 Landing Mare. *Astrophys. J. Lett.* **974**, L37 (2024).
63. Xiao, Z., Zeng, Z., Ding, N. & Molaro, J. Mass wasting features on the Moon – how active is the lunar surface?. *Earth Planet. Sci. Lett.* **376**, 1–11 (2013).
64. Wang, Y., Xie, M., Xiao, Z. & Cui, J. The minimum confidence limit for diameters in crater counts. *Icarus* **341**, 113645 (2020).
65. Palucis, M. C., Jasper, J., Garczynski, B. & Dietrich, W. E. Quantitative assessment of uncertainties in modeled crater retention ages on Mars. *Icarus* **341**, 113623 (2020).
66. Robbins, S. J. et al. Revised recommended methods for analyzing crater size-frequency distributions. *Meteorit Planet. Sci.* **53**, 891–931 (2018).
67. Crater Analysis Techniques Working Group Standard techniques for presentation and analysis of crater size-frequency data. *Icarus* **37**, 467–474 (1979).
68. Hartmann, W. K., Quantin, C., Werner, S. C. & Popova, O. Do young martian ray craters have ages consistent with the crater count system?. *Icarus* **208**, 621–635 (2010).
69. McInnes, L., Healy, J. & Astels, S. hdbscan: Hierarchical density based clustering. *JOSS* **2**, 205 (2017).
70. Robbins, S. J. et al. Craters of the Pluto-Charon system. *Icarus* **287**, 187–206 (2017).
71. Hahn, R. M. & Byrne, P. K. A Morphological and Spatial Analysis of Volcanoes on Venus. *JGR Planets* **128**, e2023JE007753 (2023.).
72. Holsapple, K. A. IMPACTS—A program to calculate the effects of a hypervelocity impact into a Solar System body. *arXiv preprint arXiv:2203.07476* (2022).
73. Schultz, P. H. & Gault, D. E. Atmospheric effects on Martian Ejecta Emplacement. *J. Geophys. Res.* **84**, 7669–7687 (1979).
74. Carlson, M. A., Melosh, H. J. & Johnson, B. C. Atmospheric Interactions of Ejecta on Earth and Mars Including the Effect of Vaporization. *Planet. Sci. J.* **4**, 194 (2023).
75. Luo, F. et al. Contemporaneous formation of self-secondaries and layered ejecta deposits on Mars. *Zenodo* <https://doi.org/10.5281/zenodo.10083548>. (2025).

## Acknowledgements

The authors are supported by the National Natural Science Foundation of China (42241108, 423B2205, 42273040, 42003053) and the Fundamental Research Funds for the Central Universities, Sun Yat-sen University (24lgzy003).

## Author contributions

F.L. and Z.X. contributed to the conceptualization, visualization, methodology, analysis and writing of the paper. R.X., Y.M., Y.C., W.C., Y.W., and J.C. joined the discussions.



## Competing interests

The authors declare no competing interests.

## Additional information

**Supplementary information** The online version contains supplementary material available at

<https://doi.org/10.1038/s43247-025-02275-4>.

**Correspondence** and requests for materials should be addressed to Zhiyong Xiao.

**Peer review information** *Communications Earth & Environment* thanks Trudi Hoogenboom, Clark Chapman and the other, anonymous, reviewer(s) for their contribution to the peer review of this work. Primary Handling Editor: Joe Aslin. [A peer review file is available].

**Reprints and permissions information** is available at <http://www.nature.com/reprints>

**Publisher's note** Springer Nature remains neutral with regard to jurisdictional claims in published maps and institutional affiliations.

**Open Access** This article is licensed under a Creative Commons Attribution-NonCommercial-NoDerivatives 4.0 International License, which permits any non-commercial use, sharing, distribution and reproduction in any medium or format, as long as you give appropriate credit to the original author(s) and the source, provide a link to the Creative Commons licence, and indicate if you modified the licensed material. You do not have permission under this licence to share adapted material derived from this article or parts of it. The images or other third party material in this article are included in the article's Creative Commons licence, unless indicated otherwise in a credit line to the material. If material is not included in the article's Creative Commons licence and your intended use is not permitted by statutory regulation or exceeds the permitted use, you will need to obtain permission directly from the copyright holder. To view a copy of this licence, visit <http://creativecommons.org/licenses/by-nc-nd/4.0/>.

© The Author(s) 2025